Faraday Discussions

Cite this: *Faraday Discuss.*, 2025, **255**, 411

ROYAL SOCIETY OF CHEMISTRY

PAPER

View Article Online
View Journal | View Issue

Tracking Li atoms in real-time with ultra-fast NMR simulations†

Angela F. Harper, *[a] Tabea Huss, [a] Simone S. Köcher [ab]
and Christoph Scheurer[a]

Received 13th April 2024, Accepted 18th April 2024

DOI: 10.1039/d4fd00074a

We present for the first time a multiscale machine learning approach to jointly simulate atomic structure and dynamics with the corresponding solid state Nuclear Magnetic Resonance (ssNMR) observables. We study the use-case of spin-alignment echo (SAE) NMR for exploring Li-ion diffusion within the solid state electrolyte material Li_3PS_4 (LPS) by calculating quadrupolar frequencies of ^{7}Li. SAE NMR probes long-range dynamics down to microsecond-timescale hopping processes. Therefore only a few machine learning force field schemes are able to capture the time- and length scales required for accurate comparison with experimental results. By using a new class of machine learning interatomic potentials, known as ultra-fast potentials (UFPs), we are able to efficiently access timescales beyond the microsecond regime. In tandem, we have developed a machine learning model for predicting the full ^{7}Li electric field gradient (EFG) tensors in LPS. By combining the long timescale trajectories from the UFP with our model for ^{7}Li EFG tensors, we are able to extract the autocorrelation function (ACF) for ^{7}Li quadrupolar frequencies during Li diffusion. We extract the decay constants from the ACF for both crystalline β-LPS and amorphous LPS, and find that the predicted Li hopping rates are on the same order of magnitude as those predicted from the Li dynamics. This demonstrates the potential for machine learning to finally make predictions on experimentally relevant timescales and temperatures, and opens a new avenue of NMR crystallography: using machine learning dynamical NMR simulations for accessing polycrystalline and glass ceramic materials.

I. Introduction

Probing dynamical effects is particularly important for energy materials, in which mobile ions drive the device functionality. The mobility of species and structural features such as disorder and defects are closely interwoven, and often are the critical factors for determining device performance. In order to establish a correlation between structure and dynamics, various experimental ssNMR

---

[a] *Fritz-Haber Institute of the Max Planck Society, Berlin, Germany. E-mail: harper@fhi.mpg.de*

[b] *Institut für Energie und Klimaforschung (IEK-9), Forschungszentrum Jülich GmbH, Jülich, Germany*

† Electronic supplementary information (ESI) available. See DOI: **https://doi.org/10.1039/d4fd00074a**

methods can be employed.[1,2] One such method is SAE NMR, which is commonly used to study Li dynamics *operando* within solid-state Li-ion battery materials.[3–6] SAE probes the quadrupolar interaction of the EFG tensor at the ^{7}Li nucleus (spin $I = 3/2$) with its local surrounding environment in order to observe the motion of Li-ions hopping between various sites in a material.

Combining static experimental ssNMR spectra with first principles density functional theory (DFT) is already an established method for elucidating structure in crystalline and amorphous battery materials.[7–11] Within the literature on NMR crystallography for battery materials, there is a primary focus on calculating chemical shielding (CSA) tensors,[8,12–15] as quadrupolar interactions are only a secondary effect, observed for nuclei with $I > 1/2$. However, there are also many DFT calculated quadrupolar parameters derived from EFG tensors, used in NMR crystallography for common quadrupolar nuclei found in battery materials, such as ^{7}Li, ^{17}O, and ^{27}Al.[10,16–21] While the calculation of static EFG tensors using DFT is a straightforward approach, a technique such as SAE requires computational methods that are capable of following dynamic processes over both long length and timescales. Studying these dynamics is of course impossible with DFT calculated ssNMR tensors (both CSA and EFG tensors), due to the computational constraints associated with the fact that DFT typically scales as $\mathcal{O}(N^3)$. Even recent applications of machine learning to NMR have been limited to static use-cases,[22] incapable of capturing dynamical or time-dependent effects. A classical approach using the Sternheimer approximation has proven successful for tracking ion motion in liquid electrolytes, where the fast ion motion reduces the requirements for computing NMR observables to picosecond timescales.[23] However, for slower ion motion (relative to the liquid state), this approach is not feasible, and therefore cannot be applied to study solid-state Li-ion motion, which requires simulations on the order of microseconds.

Fortunately, the recent introduction of machine learning inter-atomic potentials (MLIPs) has enabled simulations of such long-timescale processes within reasonable computational time and at sufficient fidelity for complex materials.[24–26] The first generation of MLIPs achieved speedups of three orders of magnitude over DFT, making nanosecond simulations possible in many cases.[27–29] Even more recently, a set of ultra-fast machine learning potentials (UFPs) was introduced[27] which provides a speedup of nearly five orders of magnitude over DFT, while maintaining the same accuracy as some of the most accurate MLIPs such as the Gaussian Approximation Potential (GAP).[28] With the UFP, it is now possible to routinely simulate up to the microsecond timescale almost at DFT accuracy.[30–33]

By using the UFP combined with a machine learning model for EFG tensors, we can now extend the capabilities of NMR crystallography to make dynamical simulations on microsecond timescales a reality. Using this UFP+ML-EFG model, we will demonstrate how to calculate the relevant ACF of quadrupolar precession frequencies for SAE experiments in the fast ion conductor Li_3PS_4 (LPS). LPS is the ideal system to study dynamic Li processes as it has both a crystalline (β-LPS) and amorphous (am-LPS) phase which are Li-ion conducting with predicted Li hopping mechanisms in the 10^5 to 10^7 s^{-1} range.[34,35] We finally show that SAE would be highly sensitive to understanding Li-ion motion in these materials on the micro-structural level, and therefore propose to use this method in combination with experimental SAE to further study the intermediate glass-ceramic LPS materials which are known to have large amounts of disorder.[36]

II. Methods

A. SAE NMR and the EFG tensor

SAE NMR is a probe of the change in the quadrupolar precession frequency (ω_Q) over time for a specific nucleus with a spin $I > 1/2$, such as ^{7}Li, which has a nuclear spin of $I = 3/2$. For the nucleus of a single Li atom, ω_Q is extracted from the EFG tensor **V**, which describes the interaction between the quadrupole of the nucleus and its surrounding electric field. The EFG tensor is the second positional derivative of the electric field **V** around the nucleus,

$$\boldsymbol{V}_{ij} = \frac{\partial^2 V}{\partial x_i \partial x_j}. \tag{1}$$

By diagonalizing the resulting tensor and finding the eigenvalues and eigenvectors, ω_Q for each ^{7}Li atom can be computed,

$$\omega_Q = \frac{1}{2} C_Q \left(3\cos^2(\theta) - 1 - \eta \sin^2(\theta)\cos(2\phi)\right). \tag{2}$$

In eqn (2), C_Q is the quadrupolar coupling constant of a single atom of ^{7}Li, which defines the magnitude of the tensor **V**, η is the asymmetry parameter which describes the shape of the tensor **V**, and θ and ϕ describe the orientation of the tensor **V** with respect to an external reference system.[37] Using DFT, it is possible to calculate an individual C_Q and ω_Q for every single Li atom in the simulation. An SAE NMR experiment measures an ensemble average of the single particle correlation functions for each Li atom within different electronic environments, which have distinct ω_Q.[3]

To generate an echo experimentally, which is proportional to the $\omega_Q(t)$, a Jeener–Broekaert pulse-sequence is used,[38,39] and the resulting $\langle \mathrm{ACF}_{\omega_Q} \rangle$, measures the phase of $\omega_Q(t = 0)$ with $\omega_Q(t = t_m)$ where t_m is the mixing time used in the pulse sequence. In the case of $I = 3/2$,[3]

$$\langle \mathrm{ACF}_{\omega_Q} \rangle = \frac{9}{20} \left\langle \sin\left(\omega_Q(t_m = 0) t_p\right) \cdot \sin\left(\omega_Q(t_m) t_d\right) \right\rangle. \tag{3}$$

The total $\langle \mathrm{ACF}_{\omega_Q} \rangle$ is calculated as an ensemble average over all the Li sites within the sample for a given pulse time t_p, decay time t_d, and mixing time t_m. In the case of a simulated $\langle \mathrm{ACF}_{\omega_Q} \rangle$, the pulse and decay time follow $\{t_p, t_d\} \to 0$, allowing us to simplify eqn (3) to[40]

$$\langle \mathrm{ACF}_{\omega_Q} \rangle \propto \langle \omega_Q(t_m = 0) \cdot \omega_Q(t_m) \rangle. \tag{4}$$

The $\langle \mathrm{ACF}_{\omega_Q} \rangle$ measures the probability of finding a Li-ion at time $t = t_m$ in a position with an equivalent ω_Q as it had at time $t = 0$. Thus, in materials in which the Li atoms visit sites with different ω_Q, the $\langle \mathrm{ACF}_{\omega_Q} \rangle$ in eqn (4) typically behaves as a decaying exponential function and one can extract the decay time τ_{SAE} directly using a stretched exponential form of the Lipari–Szabo relation,[3,41]

$$\langle \mathrm{ACF}_{\omega_Q} \rangle = b^2 + (1 - b^2) \cdot \exp(-(t_m/\tau_{\mathrm{SAE}})^{\gamma}). \tag{5}$$

The exponential Lipari–Szabo decay assumes normal translational diffusion and a random orientation of the local environment with respect to the magnetic field. This assumption holds for glasses or polymer solutions which have a random distribution of environments either due to the amorphous nature of the material or due to the tumbling motion of the polymer in a liquid.[23] In an ideal liquid with fast diffusion, the stretching factor γ is 1.0, and the exponential decays to 0. However, in complex solids, some memory of previous sites may be retained during the decay and averaging might not be complete, and therefore the exponential decays to a constant value and $\gamma < 1$ occurs *e.g.* for cases of subdiffusion as in a diffusion-trap model.[42] From the SAE decay time, τ_{SAE}, the effective Li hopping rate is then given by τ_{SAE}^{-1}.

DFT simulations access the limit of $\{t_\mathrm{p}, t_\mathrm{d}\} \rightarrow 0$, as in eqn (4) and (5), and neglect any experimental dead time, hence allowing us to naturally simulate a non-ensemble averaged $\mathrm{ACF}_{\omega_\mathrm{Q}}$ for site specific trajectories within a molecular dynamics (MD) simulation. We can therefore target processes which are faster than the lower limit of what is possible in experimental SAE, as the experiment is limited by the lower bound on the order of 10 μs, defined by t_d and t_p as well as the inverse of the quadrupolar interaction.[40,43] It is therefore possible to extract an atomistic $\mathrm{ACF}_{\omega_\mathrm{Q}}$ from an MD simulation as long as one can calculate the EFG tensors for all Li atoms across every snapshot of the simulation. A single snapshot of the MD simulation with ω_Q and C_Q calculated for each individual atomic site from DFT is the equivalent of the 0 K temperature limit, in which all motion in the system is frozen and all ions remain in their initial site. Under realistic room temperature experimental conditions for SAE, the quadrupolar observables are averaged ($\bar{C}_\mathrm{Q}$ and $\bar{\omega}_\mathrm{Q}$), not only over the fast timescale hopping events which are masked in experiment but also over thermal effects and different Li sites.

B. Ultra-fast potentials

Studying timescales relevant for spin alignment measurements necessitates an efficient methodology for the evaluation of energies and forces to drive molecular dynamics over microsecond timescales. Xie *et al.* have recently introduced a new interatomic potential, matching the accuracy of established MLIPs but boosting the speed by one or two orders of magnitude, such that it is comparable with the computational efficiency of classical force-fields.[27] The architecture uses a local representation of atomic environments as established by fundamental work using SOAP and Behler–Parrinello symmetry functions.[44,45]

The energy of the system is expanded as a sum of 2-body and 3-body contributions using cubic B-splines, which combine the beneficial properties of smoothness and differentiability with the advantage of a compact support. Hence, the number of basis functions that need to be evaluated in every energy computation step is strongly limited, as a maximum of four functions can be nonzero in every segment. The low number of basis functions directly relates to a high computational efficiency.[27]

The UFP is trained using the active learning procedure shown in the workflow in Fig. 1A. The initial dataset is an existing set of LPS structures which was used to train a GAP[28] for LPS.[31] The UFP is trained and iteratively improved by adding structures of β- and am-LPS to the training set. Structures are drawn from UFP-MD simulations, where the UFP used for each iteration is the most recent UFP

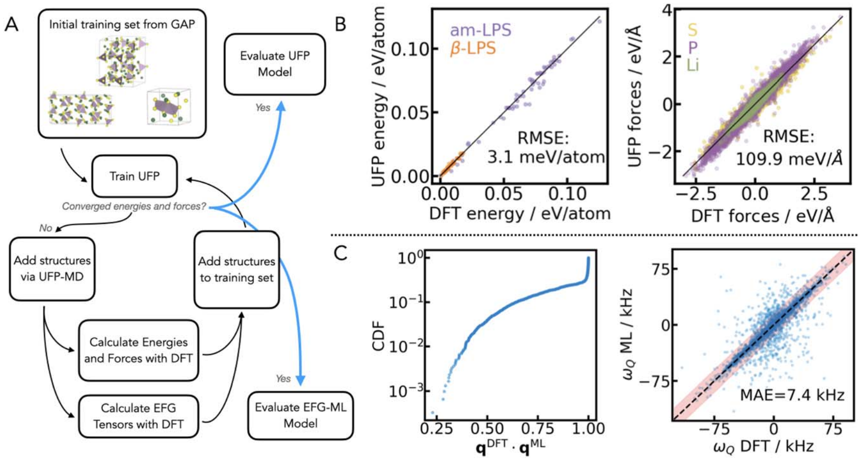

Fig. 1 Workflow of the UFP+ML-EFG training. The left panel shows the active learning workflow (A) starting from a set of structures used to train a GAP[28] for LPS[31] to the final training of the UFP (B) and ML-EFG model (C). The UFP has an RMSE in the energies of 3.1 meV per atom and forces of 109.9 meV Å^{-1}. The ML-EFG model is assessed both by the quality of the relative orientation of the tensors and the MAE in ω_Q. C shows the combined distribution function (CDF) of the quaternion scalar product between the DFT and ML quaternions, $\mathbf{q}^{DFT}\cdot\mathbf{q}^{ML}$. This indicates that the majority of tensors are oriented in the same direction comparing DFT to ML. The ML-EFG model has an error of 7.4 kHz on ω_Q, where the experimental sensitivity of ^{7}Li SAE (10 kHz) is shown shaded in red.

obtained during the training workflow. This active learning cycle of training, UFP-MD simulation, and model evaluation is repeated iteratively until convergence of the UFP energy and force errors is achieved. Finally, the converged energy and forces over a withheld test set are displayed in Fig. 1B (3.1 meV per atom and 109.9 meV Å^{-1}, respectively). These are comparable with the corresponding errors for the GAP for LPS.[31] In addition to the iterative training procedure used to create a robust dataset, the hyperparameters specific to the UFP model were also optimized. Details are given in the ESI Table 1.†

C. An ML model for EFG tensors

The Symmetry Adapted Gaussian Process Regression (SA-GPR) machine learning framework, combines covariant atomic descriptors with symmetry adapted kernels in order to learn tensors of any dimension with Gaussian process regression.[46] We have previously shown that by using tensorial learning *via* the SA-GPR framework, we are able to predict quadrupolar frequencies (ω_Q) for the ^{7}Li nucleus within the experimental sensitivity of SAE NMR.[47] We couple the workflow for tensorial learning to the active learning procedure used for training the UFP, as shown in Fig. 1A, in order to train a model for predicting the ^{7}Li EFG tensors of β- and am-LPS. The final set of structures from the active learning procedure for the UFP is used as the training set for validating the ML-EFG model.

The final set of DFT computed ^{7}Li EFG tensors over structures of Li_3PS_4 contains 166 diverse structures from the LPS UFP model, which have a total of 14 448 Li environments. The EFG tensor for each atom is calculated for all the structures using the plane-wave pseudopotential DFT code CASTEP v22.[48,49] The hyperparameters for the SA-GPR descriptor are optimized as described in the ESI,† using a 5-fold cross validation procedure with a test set, which is withheld from training. The resulting mean absolute error (MAE) for the test set in ω_Q is 7.4 kHz, and the correlation plot is shown in Fig. 1C. It is important to note that the density of points of ω_Q within the red bar is high, and thus this representation highlights the outliers as they are clearer to distinguish from the majority.

In addition to evaluating the MAE in ω_Q, it is also important to validate how well the ML-EFG model predicts the orientation of the ^{7}Li EFG tensors. Besides magnitude (C_Q) and shape (η), the $\langle \mathrm{ACF}_{\omega_Q} \rangle$ is a sensitive measure of the orientation of one tensor at a time t_m relative to another at t_0. We use the unit quaternion $\mathbf{q}$ to uniquely define the orientation of each tensor.[47,50] The unit quaternion is a superior metric for determining orientation over Euler angles, as it is independent of the choice of reference system. Therefore, in Fig. 1C, we show the cumulative distribution function (CDF) of the scalar product between the DFT calculated and ML-EFG predicted quaternions, $\mathbf{q}^{\mathrm{DFT}} \cdot \mathbf{q}^{\mathrm{ML}}$. A scalar product of 1 indicates perfect alignment, and from Fig. 1C, we see that around 75% of the predicted EFG tensors are well aligned with their DFT reference ($\mathbf{q}^{\mathrm{DFT}} \cdot \mathbf{q}^{\mathrm{ML}} \geq 0.9$). This is an important factor as it will reduce the noise in the $\langle \mathrm{ACF}_{\omega_Q} \rangle$, eqn (4).

We finally test the ML-EFG model for size extensivity, because the system sizes included in the training set are between 200 and 256 atoms per unit cell, due to DFT performance considerations, while our target structures for β-LPS and am-LPS are 384 and 576 atoms, respectively. Therefore, we calculated the EFG tensors using DFT for two structures of β- and am-LPS each, extracted from the final 1 μs UFP simulations, and predicted the ^{7}Li EFG tensors for these four structures using the ML-EFG model (see ESI Fig. S2†). The accuracy of the ω_Q parameter for these four larger models is 9.2 kHz, which is below the experimentally known sensitivity of ^{7}Li SAE experiments of about 10 kHz. Thus, we can say with confidence that our model will have reasonable accuracy on the larger system sizes used in the final 1 μs UFP simulations.

III. Results

A. Microsecond simulations with UFPs

In addition to the low energy and force errors of the UFP shown in Fig. 1, it is also important to validate the behavior of the UFP relative to high quality first principles methods. Therefore, we compare the structural models generated using the UFP with literature models generated from *ab initio* molecular dynamics (AIMD). The radial distribution function (RDF) for β-LPS and am-LPS in a 300 K, 1 μs simulation with the UFP is shown in the ESI, Fig. S5,† in comparison with two literature references for the RDF of β- and am-LPS from AIMD.[51,52] The UFP simulated RDFs for both β- and am-LPS show excellent agreement with AIMD. We also compare the UFP with the established method of Turbo-GAP[53] for β-LPS and am-LPS using the mean square displacement (MSD) at 500 K (see Fig. S6 in the ESI†). We reach a perfect agreement for the am-LPS and a deviation of a factor of five for the β-LPS. The deviation can be explained with a much higher sensitivity of the MSD on the barrier height and density in the crystalline material and could potentially be improved by extending the dataset with additional nudged elastic band calculations over Li hopping events.

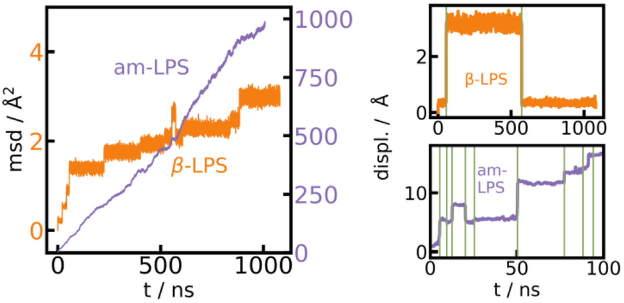

Fig. 2 MSD for β-LPS and am-LPS using the UFP. MSD of am-LPS and β-LPS (left), showing that transport is roughly two orders of magnitude faster in the amorphous material. A showcase of hopping detection (right) from the absolute displacement in the case of β-LPS (top) and am-LPS (bottom), hops are marked with green lines.

Furthermore, we can extract the average hopping rate of Li-ions by discretizing the MSD of all independent single ion trajectories (details of the discretization procedure are given in the ESI†) (Fig. 2). From the discretized trajectories, we calculate Li hopping rates of $2.57 \times 10^5\ \mathrm{s}^{-1}$ for β-LPS and $7.0 \times 10^7\ \mathrm{s}^{-1}$ for am-LPS. Our results of significantly faster ion diffusion in am-LPS than in the crystalline β-LPS phase are in line with our previous findings and experimental reports.[31,54,55]

Finally, as a result of using the UFP, we are able to simulate dynamics at 300 K for 1 μs. To the best of our knowledge, simulations of this length have not yet been executed using MLIPs. Typical simulation times with MLIPs are on the order of nanoseconds, reaching 100 ns at most.[56] Additionally, most previous studies use higher temperatures in their MD runs,[31,57,58] which induces an extrapolation error in their property prediction at room temperature. With an established methodology like the Turbo-GAP, a 1 μs MD simulation would require on the order of 1 million CPUh. With an acceleration factor of 25 over TurboGAP, the UFP-MD for LPS on the other hand was computationally feasible in a couple of weeks (40 000 CPUh on a single compute node).

B. ACF for quadrupolar frequencies

Using the UFP+ML-EFG model, we obtain the $\langle \mathrm{ACF}_{\omega_Q} \rangle$ over a 1 μs simulation at 300 K run using the UFP for both β- and am-LPS, as shown in Fig. 3. The $\langle \mathrm{ACF}_{\omega_Q} \rangle$ is averaged over all Li atoms in each system, and normalized to [0,1].

1. β-LPS. As shown in Fig. 3, there is no visible decay present in the $\langle \mathrm{ACF}_{\omega_Q} \rangle$ of β-LPS at 300 K. Therefore the $\langle \mathrm{ACF}_{\omega_Q} \rangle$ could not be fit using eqn (5). This result is expected, and occurs for two reasons.

Firstly, and perhaps most importantly, we are simulating an infinite, pristine, single crystal, by imposing periodic boundary conditions over the unit cell of β-LPS. Because SAE can only distinguish between sites with an inequivalent average local EFG,[3] if Li hopping events only occur between sites with equivalent average EFGs ($\bar{\omega}_Q(t_1) = \bar{\omega}_Q(t_2)$), the $\langle \mathrm{ACF}_{\omega_Q} \rangle$ will not exhibit the characteristic exponential decay. While this would usually be associated with vanishing mobility (which is not the case in β-LPS as shown in Fig. 2 left), it can also be due to insensitivity of

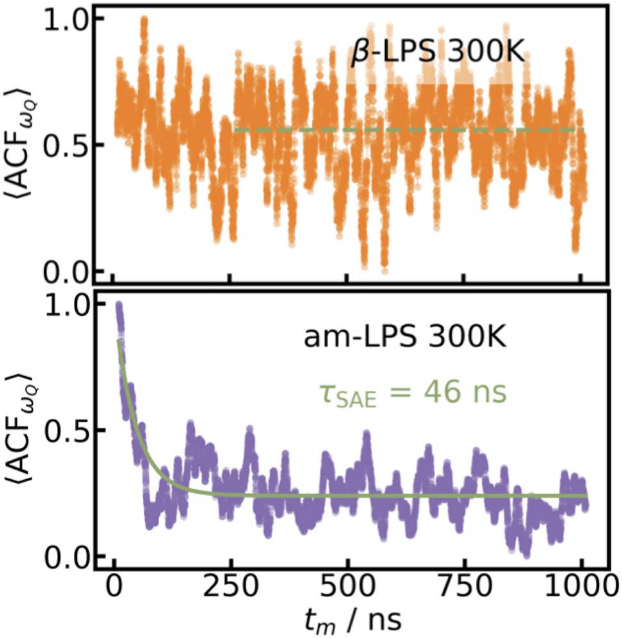

Fig. 3 $\langle ACF_{\omega_Q} \rangle$ for β-LPS and am-LPS. The $\langle ACF_{\omega_Q} \rangle$ given by eqn (4) calculated over a 1 μs UFP-MD simulation at 300 K for 144 Li atoms in single-crystalline β-LPS (top, orange) and 216 Li atoms in am-LPS (bottom, purple). A decay time, $\tau_{SAE} = 46$ ns, can be extracted from the am-LPS $\langle ACF_{\omega_Q} \rangle$.

SAE with respect to motion between equivalent $\bar{\omega}_Q$. Thus, if there are a few sets of mutually inequivalent sites with similar $\bar{\omega}_Q$ one would obtain a partially averaged $\bar{\omega}_Q$,[43] which is the weighted average between the $\bar{\omega}_Q$ for each of these sites. A single crystal, therefore, will always be such a case, because all of the sites have the same predominant orientation throughout the simulation. A slow decay, beyond the microsecond timescale, would be dominated in a polycrystalline material by Li motion across grain boundaries of differently oriented crystalline grains. In this case, the τ_{SAE} decay could be modeled as a function of the Li diffusion coefficient and grain size distribution.

Secondly, in this particular example of β-LPS, there are only two crystallographically inequivalent Li sites, a tetrahedral LiS_4 site and an octahedral LiS_6 site, which possess almost identical local $\bar{\omega}_Q$. We can show this by looking at a distribution of the DFT calculated ω_Q values of all the crystalline β-LPS structures included in the training set for our ML-EFG model, shown in the left panel of Fig. 4. The distributions are fairly narrow and the average $\bar{\omega}_Q$ for LiS_4 is 10.8 kHz, and for LiS_6 $\bar{\omega}_Q$ is 13.8 kHz, a difference of less than 4 kHz. A close look at the first 250 ns of the β-LPS $\langle ACF_{\omega_Q} \rangle$ suggests that there is a small initial decay due to the inverse jump rate between LiS_4 and LiS_6 sites, which is undetectable due to both the signal-to-noise ratio of the $\langle ACF_{\omega_Q} \rangle$ as a result of the overlap in ω_Q between the sites, as well as the low number of Li sites (144 total) in the β-LPS unit cell. This could likely be resolved in the model with a larger sampling of trajectories, but is not relevant for the observable quantities in the SAE experiment,

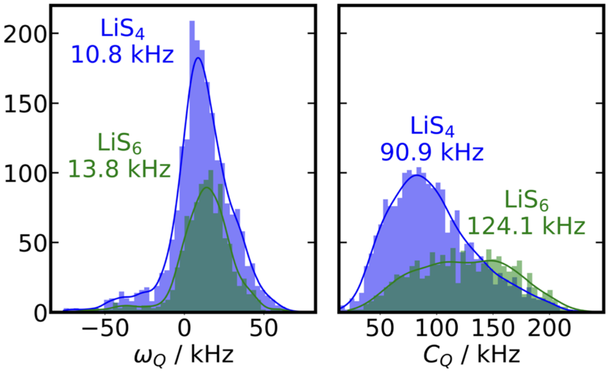

Fig. 4 Distributions of ω_Q and C_Q in β-LPS. The left panel shows the distribution of tetrahedral LiS_4 sites (blue) to octahedral LiS_6 sites (green), calculated using DFT, for the crystalline β-LPS structure. The right panel uses the same color scheme to show the distributions of C_Q sites for β-LPS. C_Q and ω_Q are calculated for all 33 β-LPS structures in the ML-EFG model.

where one would observe the residual, partially averaged coupling, shown in green in Fig. 3.

To highlight the intricate relationship between tensor shape and orientation in β-LPS that leads to the very similar and narrow ω_Q distributions displayed in Fig. 4 (left) we also compute a theoretical autocorrelation function $\langle \mathrm{ACF}_{C_Q} \rangle$ of the orientation-independent coupling constant, C_Q, experienced by the Li ions during their motion through the crystalline model in the MD simulation. We note that this is not a directly accessible quantity in the SAE experiment.[59] We compute this $\langle \mathrm{ACF}_{C_Q} \rangle$ in a similar fashion to that for ω_Q given in eqn (4),

$$\langle \mathrm{ACF}_{C_Q} \rangle \propto \langle C_Q(t_m = 0) \cdot C_Q(t_m) \rangle, \tag{6}$$

and fit the resulting $\langle \mathrm{ACF}_{C_Q} \rangle$ over the stretched exponential given by eqn (5) to extract a decay constant τ and Li hopping rate τ^{-1}.

A histogram of all of the individual atomistic C_Q values calculated using DFT on the β-LPS training set is shown in Fig. 4, right panel. The spread of C_Q values for the LiS_6 sites is much wider than that for LiS_4, and their averages are able to be discriminated (a 30 kHz difference). LiS_6 sites have an average $\bar{C}_Q$ of 124.1 kHz, whereas LiS_4 sites have an $\bar{C}_Q$ of 90.9 kHz. Thus while $\bar{\omega}_Q$ cannot be used to distinguish these two sites, their $\bar{C}_Q$ values could be a good target to understand the local structure in ideal single crystal β-LPS.

Using the UFP-MD, we are able to track single-atom trajectories across the simulation, and therefore can calculate a single-atom ACF_{C_Q}, for each site in the β-LPS crystalline structure. In order to understand how the $\langle \mathrm{ACF}_{C_Q} \rangle$ behaves, we separate the individual single atom ACF_{C_Q}, by the Li sites at time $t = 0$. In Fig. 5, we plot both the individual ACF_{C_Q} and $\langle \mathrm{ACF}_{C_Q} \rangle$, where the individual ACF_{C_Q} are colored by the site in which the Li atom started at time $t = 0$. The $\langle \mathrm{ACF}_{C_Q} \rangle$ average is calculated over the 13 Li ions that experience a hop to a different site (either $LiS_4 \rightarrow LiS_6$ or *vice versa*) during the 1 μs simulation, to reduce the noise in the $\langle \mathrm{ACF}_{C_Q} \rangle$. We show that averaging over only the sites which hop is a reasonable

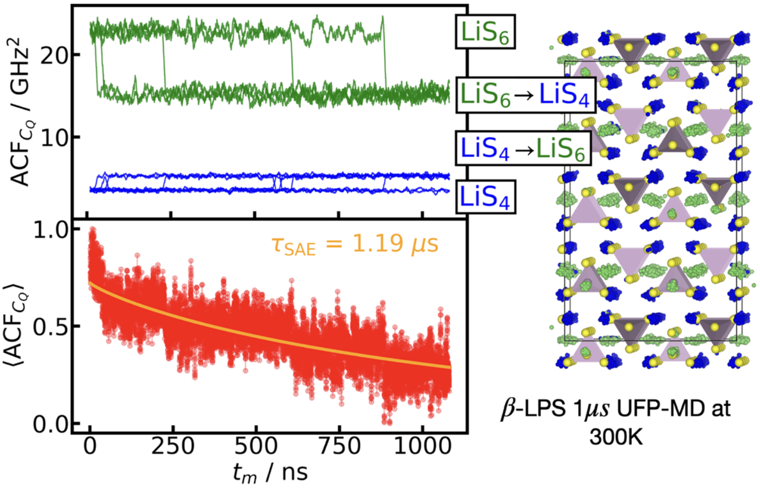

Fig. 5 $\langle \mathrm{ACF}_{C_Q} \rangle$ for β-LPS. By considering only the Li atoms in the 300 K simulation which perform a hop to another site during the 1 μs simulation (either $\mathrm{LiS_4} \rightarrow \mathrm{LiS_6}$ or $\mathrm{LiS_6} \rightarrow \mathrm{LiS_4}$), and calculating the $\langle \mathrm{ACF}_{C_Q} \rangle$ over these sites, we extract τ of 1.19 μs. The colors of the individual atom ACF_{C_Q} shown in the top left panel correspond to the starting site of the Li atom at time $t = 0$. Thus $\mathrm{LiS_6}$ sites at $t = 0$ which hop to $\mathrm{LiS_4}$ sites have an ACF_{C_Q} in green, and $\mathrm{LiS_4}$ sites at $t = 0$ which hop to $\mathrm{LiS_6}$ sites are shown in blue. The trajectories of all Li atoms are colored in the same fashion in the right panel of the Li atoms trajectory.

assumption to make by comparing these results to a 1 μs simulation at 350 K, shown in the ESI Fig. S3,† in which 102 Li atoms hop during the simulation, and there is better averaging over more sites.

From the top panel in Fig. 5, we can clearly distinguish the individual ACF_{C_Q} for $\mathrm{LiS_6}$ sites (green), $\mathrm{LiS_4}$ sites (blue), and hopping events between the sites, as there is a steep rise (or drop) in the ACF_{C_Q} at each hopping event. Taking the average over all 13 Li sites, the $\langle \mathrm{ACF}_{C_Q} \rangle$ does exhibit an exponential decay. Fitting the $\langle \mathrm{ACF}_{C_Q} \rangle$ in Fig. 5 to eqn (5), we find a decay time of $\tau = 1.19$ μs, or a Li hopping rate of $8.41 \times 10^5\ \mathrm{s}^{-1}$. This is on the same order of magnitude as the Li hopping rate extracted from the MSD, $2.57 \times 10^5\ \mathrm{s}^{-1}$. Additionally, by removing the orientation dependence, and averaging over only the hopping sites, we achieve better signal to noise ratio, and can more clearly distinguish the small initial decay at ($t_\mathrm{m} < 50$ ns).

2. **am-LPS.** In contrast to the β-LPS $\langle \mathrm{ACF}_{\omega_Q} \rangle$, which exhibits no exponential decay, as shown in Fig. 3, the $\langle \mathrm{ACF}_{\omega_Q} \rangle$ for am-LPS shows a clear, fast exponential decay which can be fit to the Lipari–Szabo relation[41] given in eqn (5) ($\gamma = 1.0$). The decay time extracted from $\langle \mathrm{ACF}_{\omega_Q} \rangle$ for am-LPS is $\tau_\mathrm{SAE} = 46$ ns, which corresponds to a Li hopping rate of $\tau_\mathrm{SAE}{}^{-1} = 2.17 \times 10^7\ \mathrm{s}^{-1}$. Comparing this with the hopping rate extracted from the MSD ($7.0 \times 10^7\ \mathrm{s}^{-1}$), we see that both methods predict the same order of magnitude hopping rates for Li at 300 K. The hopping rate extracted from $\tau_\mathrm{SAE}{}^{-1}$ is a slight underestimation to the rate extracted from the MSD, however this is consistent with the fact that the $\langle \mathrm{ACF}_{\omega_Q} \rangle$ is not sensitive to all ion hops that occur within the material, only those for which $\omega_{t_\mathrm{m}} \neq \omega_{t_0}$, as discussed above.

Previous work on Li hopping in LPS using a 100 ps AIMD simulation of am-LPS with 48 Li atoms at 600 K, predicts Li hopping rates in the range of 10^{11} s^{-1}.[60] Their method for determining a Li hopping event involved tracking the escape time for Li atoms to leave a 3 Å radius surrounding the nearest polyanion and fitting this escape mechanism to an exponential decay function. Given the short timescale of the simulation, they were only able to access hopping events with residence times shorter than 100 ps (10^{10} s^{-1}). As the shortest $\tau_{SAE} = 46$ ns, for real ion hops in am-LPS, this requires a simulation of at least several nanoseconds at 300 K considering the signal-to-noise ratio in the simulation to accurately estimate the hopping rate. This highlights the importance of simulating both at room temperature and for a sufficiently long simulation time, in order to achieve convergence of the Li dynamics and observe the correct motion of Li atoms within LPS. Similar inaccuracies from simple extrapolation to ambient conditions are expected for any material with broad and complex distributions of migration barriers that become progressively accessible upon temperature increase.

IV. Discussion

This study pioneers the application of the latest generation of machine learning techniques to directly predict dynamical ssNMR observables at microsecond timescales from atomistic simulations. It is important to stress that an ssNMR calculation with DFT accuracy on the μs timescale would not be possible without leveraging machine learning to predict the EFG tensors. Calculating EFG tensors for the 576 atom am-LPS unit cell over a 1 μs simulation would cost roughly 22.5 million CPUh, with snapshots taken every 100 ps. The same prediction made using the ML-EFG model uses 500 CPUh. This is a factor of 45 000 speedup over DFT-calculated EFG tensors. Therefore, this is, to the best of our knowledge, the first dynamical ssNMR calculation performed at DFT level accuracy, and on an experimentally relevant timescale.

By integrating first-principles methodologies, it ensures consistent multiscaling between NMR calculations derived from DFT and predictions applied to large-scale structures. Unlike AIMD studies on Li-ion conduction and diffusivity, where high temperatures are necessary in order to promote ion motion and gather enough statistics, we are able to simulate LPS at 300 K, which is the relevant temperature for comparison with realistic experimental solid state electrolyte systems.

By calculating $\langle \mathrm{ACF}_{\omega_Q} \rangle$ in both β- and am-LPS, we find that the decay time for Li in am-LPS at 300 K is on the order of 46 ns, while the $\langle \mathrm{ACF}_{\omega_Q} \rangle$ of single-crystalline β-LPS exhibits no characteristic exponential decay, and instead oscillates about an average value of $\langle \mathrm{ACF}_{\omega_Q} \rangle$. By considering the orientations of the EFG tensors during the simulations in both β-LPS and am-LPS we can see more clearly the differences in behavior of the EFG tensor in these two materials. Fig. 6 shows a 2D histogram of all of the accessed angles during the full 1 μs simulation at 300 K for β- and am-LPS. In the β-LPS histogram (Fig. 6 left), the majority of the angles (θ, ϕ) are clustered around either (π/2, 0) for LiS_4 tetrahedra or (π/2 ± π/6, ±π/4) for LiS_6. On the other hand, there are no clear preferred values of (θ, ϕ) for am-LPS, indicating that the Li atoms experience a wide array of environments during the 1 μs simulation. The large spread in angular distribution in the am-LPS case is what leads to the characteristic rapid decay shown in Fig. 3, as the Li ions visit sites

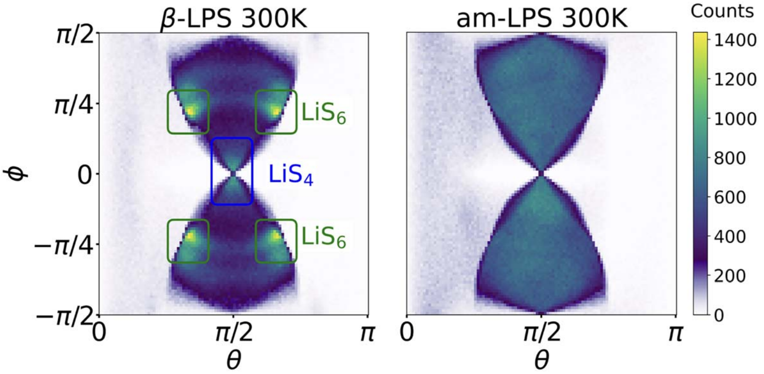

Fig. 6 Heatmap θ and ϕ distributions in β- and am-LPS. The heatmaps show the concentration of the angles θ and ϕ across the full 1 µs UFP-MD trajectory. The distributions are colored by the total number of sites with that combination of angles (θ, ϕ), and in β-LPS the angle pairs which arise from LiS_4 and LiS_6 sites are indicated.

with all possible orientations during the full simulation, leading to loss of correlation, which is normally characteristic of SAE in glasses or polymers.[23,61] Once Li atoms are in a single crystalline grain, this orientational memory loss is no longer possible, and we see slow, or nonexistent decay as in β-LPS.

We assessed the two limits of overall microstructure in the LPS fast ion conductors. The β-LPS crystal represents an infinitely large, fully uniform single crystal of LPS, as depicted in orange in Fig. 7. As such, all the ω_Q values in both

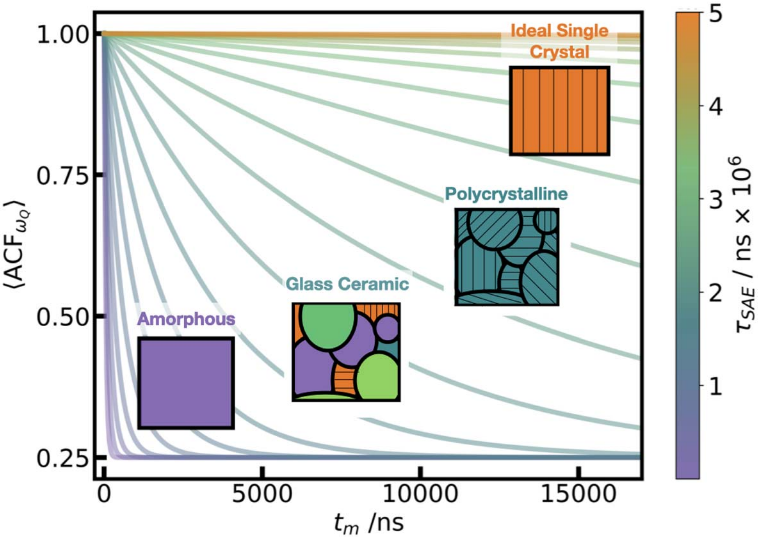

Fig. 7 Schematic of range of crystalline to amorphous τ_{SAE}. The plot shows a range of decay functions, eqn (5), with τ_{SAE} from 50 ns to 5 million ns. The inset figures show schematics of the expected microscale structure at each of these varying decay rates, with black lines in the glass ceramic and polycrystalline denoting different grains.

LiS_4 and LiS_6 sites have the same predominant value (*c.f.* Fig. 4 left), which does not vary throughout the simulation, even during Li hopping events. In addition, the mean $\bar{\omega}_Q$ for LiS_4 and LiS_6 are only 4 kHz apart, and the spread of the individual atomic ω_Q for LiS_6 is entirely contained within the distribution for LiS_4, as presented in Fig. 4. Therefore, we would expect a vanishingly small decay of $\langle ACF_{\omega_Q} \rangle$ for single crystal β-LPS, in which only those two sites are accessible, and then observe a residual, partially averaged coupling throughout. However in a polycrystalline material, shown in green in Fig. 7, where LiS_4 and LiS_6 sites are oriented along different crystal axes in neighboring grain boundaries, we are no longer limited by the predominant orientation of the ideal single crystal. In this case, we would expect lower τ_{SAE}, and a better sensitivity to inter-grain Li-ion motion for SAE.

At the other extreme, we consider the bulk am-LPS, represented by the unstructured purple square in Fig. 7, and find that $\langle ACF_{\omega_Q} \rangle$ decays rapidly over a period of 46 ns. In the homogeneous amorphous regime, we can see that as the amorphous PS_4 backbone changes across the simulation, Li atoms experience continually changing electronic environments, and thus we can think of the Li atoms moving in a "glass-like" ensemble of sites embedded in PS_4 environments. At a 46 ns decay rate, τ_{SAE} is outside of the range detectable by a real SAE experiment which would, at best, yield a small residual coupling $b^2 > 0$ (see eqn (5)). In a fast ion conductor, we expect this rapid decay of the $\langle ACF_{\omega_Q} \rangle$, however this is the first time we are able to accurately quantify the rate of this decay in an amorphous material, highlighting the importance of this UFP+ML-EFG approach.

These two regimes (single crystal and fully amorphous), which are straightforward to simulate, are not representative of the realistic microstructure in glass-ceramic LPS electrolytes.[36] All of the glass ceramic materials that are critical for building the next generation of all solid state batteries such as LISCION, LIPON, LGPS, and LPS[62] lie within this range between fully amorphous to fully crystalline Li-ion conductors with hypothetical τ_{SAE} decay constants schematically depicted in Fig. 7. That is, they are a mixture of glassy regions and crystalline regions (depicted as the glass ceramic and polycrystalline in Fig. 7), in which the Li-ion conductivity across grain boundaries is often the determining factor for the quality of these super-ionic conductors. In these cases, we propose that SAE will provide a unique grain-boundary sensitive technique for understanding Li-ion diffusion, as the intra-grain diffusion will be at either the amorphous or crystalline limit, and therefore undetectable with SAE.

Experimentally, the Granwehr group has observed $\tau_{SAE} \approx 30$–50 ms (ref. 63) in a polycrystalline sample of β-LPS, which is well above the intra-grain decay rates we have predicted here. This can likely be rationalized by sufficiently fast ($\tau \leq 1$ μs) intra-grain diffusion leading to partially averaged coupling tensors, combined with long timescale inter-grain diffusion processes between the polycrystalline grains ($\tau_{SAE} \approx$ ms). However, determining the rates and mechanisms of these processes which combine to give an experimental decay rate in the ms time scale, requires dynamical NMR crystallography and analysis techniques that allow one to unfold the various timescales and effective partially averaged interaction tensors contained in the measured data.[59] From this point onward, we now have the capability to make such an approach, by combining dynamical ssNMR with data analysis and simulations to interpret the unfolded data in terms of atomistic processes.

Beyond suggesting further work on grain-boundary simulations, we demonstrate the potential to access Li-ion motion even in single crystals, by deriving $\langle \mathrm{ACF}_{C_Q} \rangle$ and calculating a corresponding τ, which does exhibit a decay at 300 K for β-LPS. Furthermore, we show that the Li hopping rate predicted by τ^{-1} from $\langle \mathrm{ACF}_{C_Q} \rangle$ is comparable with that calculated from the β-LPS MSD.

We are just at the beginning of this new era of NMR crystallography in which we are able to accurately model dynamical processes at the same temperatures and timescales as experiment. This workflow combining UFPs and experimental observables is a baseline on which the next generation of machine learning for materials methods can be based. We are now one step closer to bridging the gap between theory and experiment, and can tackle more dynamic *operando* calculations, which were previously computationally infeasible.

Author contributions

Angela F. Harper: data curation, formal analysis, investigation, methodology, visualization, project administration, writing – original draft, writing – review and editing; Tabea Huss: data curation, formal analysis, investigation, visualization, writing – original draft; Simone S. Köcher: conceptualization, supervision, writing – review and editing; Christoph Scheurer: conceptualization, supervision, funding acquisition, writing – review and editing.

Conflicts of interest

There are no conflicts of interest to declare.

Acknowledgements

All the authors would like to thank Prof. Dr Josef Granwehr for scientific exchange and discussions regarding experimental SAE. All computational resources were provided by the Max Planck Computing and Data Facility (MPCDF). AFH would like to acknowledge the support of the Alexander von Humboldt Foundation. TH acknowledges funding by the Deutsche Forschungsgemeinschaft (DFG, German Research Foundation) within the cluster of excellence EXC 2089: e-conversion. CS acknowledges funding by the Bundesministerium für Bildung und Forschung (BMBF) within the project AdamBatt2 (FKZ 03XP0558D). Open Access funding provided by the Max Planck Society.

References

1 K. Märker, C. Xu and C. P. Grey, Operando NMR of NMC811/graphite lithium-ion batteries: structure, dynamics, and lithium metal deposition, *J. Am. Chem. Soc.*, 2020, **142**, 17447.

2 M. Gombotz and H. M. R. Wilkening, Fast Li ion dynamics in the mechanosynthesized nanostructured form of the solid electrolyte Li_3YBr_6, *ACS Sustainable Chem. Eng.*, 2021, **9**, 743.

3 M. Wilkening and P. Heitjans, From micro to macro: Access to long-range Li^+ diffusion parameters in solids via microscopic $^{6,7}Li$ spin-alignment echo NMR spectroscopy, *ChemPhysChem*, 2012, **13**, 53.

4 C. Yu, S. Ganapathy, E. R. H. v. Eck, H. Wang, S. Basak, Z. Li and M. Wagemaker, Accessing the bottleneck in all-solid state batteries, lithium-ion transport over the solid-electrolyte-electrode interface, *Nat. Commun.*, 2017, **8**, 1086.

5 K. Hogrefe, N. Minafra, W. G. Zeier and H. M. R. Wilkening, Tracking ions the direct way: long-range Li^+ dynamics in the thio-LISICON family Li_4MCh_4 (M = Sn, Ge; Ch = S, Se) as probed by ^{7}Li NMR relaxometry and ^{7}Li spin-alignment echo NMR, *J. Phys. Chem. C*, 2021, **125**, 2306.

6 B. Gadermaier, K. Hogrefe, P. Heitjans and H. M. R. Wilkening, Direct assessment of ultralow Li^+ jump rates in single crystalline Li_3N by evolution-time-resolved ^{7}Li spin-alignment echo NMR, *Eur. J. Inorg. Chem.*, 2021, **2021**, 1028.

7 S. E. Ashbrook and D. M. Dawson, Exploiting periodic first-principles calculations in NMR spectroscopy of disordered solids, *Acc. Chem. Res.*, 2013, **46**, 1964.

8 S. E. Ashbrook and D. McKay, Combining solid-state NMR spectroscopy with first-principles calculations–a guide to NMR crystallography, *Chem. Commun.*, 2016, **52**, 7186.

9 C. Szczuka, B. Karasulu, M. F. Groh, F. N. Sayed, T. J. Sherman, J. D. Bocarsly, S. Vema, S. Menkin, S. P. Emge, A. J. Morris, *et al.*, Forced disorder in the solid solution Li_3P–Li_2S: a new class of fully reduced solid electrolytes for lithium metal anodes, *J. Am. Chem. Soc.*, 2022, **144**, 16350.

10 A. F. Harper, S. P. Emge, P. C. Magusin, C. P. Grey and A. J. Morris, Modelling amorphous materials via a joint solid-state NMR and X-ray absorption spectroscopy and DFT approach: application to alumina, *Chem. Sci.*, 2023, **14**, 1155.

11 A. F. Harper, M. L. Evans, J. P. Darby, B. Karasulu, C. P. Koçer, J. R. Nelson and A. J. Morris, Ab initio structure prediction methods for battery materials: A review of recent computational efforts to predict the atomic level structure and bonding in materials for rechargeable batteries, *Johnson Matthey Technol. Rev.*, 2020, **64**, 103.

12 J. E. Frerichs, J. Koppe, S. Engelbert, L. Heletta, G. Brunklaus, M. Winter, G. K. Madsen and M. R. Hansen, ^{119}Sn and ^{7}Li solid-state NMR of the binary Li–Sn intermetallics: structural fingerprinting and impact on the isotropic ^{119}Sn shift via DFT calculations, *Chem. Mater.*, 2021, **33**, 3499.

13 I. G. Shenderovich, Experimentally established ^{15}N NMR absolute shielding scale for theoretical calculations, *J. Phys. Chem. A*, 2023, **127**, 5547.

14 E. Chaloupecká, V. Tyrpekl, K. Bártová, Y. Nishiyama and M. Dračínský, NMR crystallography of amino acids, *Solid State Nucl. Magn. Reson.*, 2024, **130**, 101921.

15 S. S. Köcher, P. Schleker, M. Graf, R.-A. Eichel, K. Reuter, J. Granwehr and C. Scheurer, Chemical shift reference scale for Li solid state NMR derived by first-principles DFT calculations, *J. Magn. Reson.*, 2018, **297**, 33.

16 S. E. Ashbrook and S. Sneddon, New methods and applications in solid-state NMR spectroscopy of quadrupolar nuclei, *J. Am. Chem. Soc.*, 2014, **136**, 15440.

17 M. M. Islam and T. Bredow, Lithium diffusion pathways in β-Li_2TiO_3: a theoretical study, *J. Phys. Chem. C*, 2016, **120**, 7061.

18 M. T. Dunstan, J. M. Griffin, F. Blanc, M. Leskes and C. P. Grey, Ion dynamics in Li_2CO_3 studied by solid-state NMR and first-principles calculations, *J. Phys. Chem. C*, 2015, **119**, 24255.

19 O. E. Zeman, I. L. Moudrakovski, C. Hartmann, S. Indris and T. Bräuniger, Local electronic structure in AlN studied by single-crystal ^{27}Al and ^{14}N NMR and DFT calculations, *Molecules*, 2020, **25**, 469.

20 E. N. Bassey, P. J. Reeves, I. D. Seymour and C. P. Grey, ^{17}O NMR spectroscopy in lithium-ion battery cathode materials: challenges and interpretation, *J. Am. Chem. Soc.*, 2022, **144**, 18714.

21 I. D. Seymour, D. S. Middlemiss, D. M. Halat, N. M. Trease, A. J. Pell and C. P. Grey, Characterizing oxygen local environments in paramagnetic battery materials via ^{17}O NMR and DFT calculations, *J. Am. Chem. Soc.*, 2016, **138**, 9405.

22 M. C. Venetos, M. Wen and K. A. Persson, Machine learning full NMR chemical shift tensors of silicon oxides with equivariant graph neural networks, *J. Phys. Chem. A*, 2023, **127**, 2388.

23 I. Chubak, L. Alon, E. V. Silletta, G. Madelin, A. Jerschow and B. Rotenberg, Quadrupolar ^{23}Na^{+} NMR relaxation as a probe of subpicosecond collective dynamics in aqueous electrolyte solutions, *Nat. Commun.*, 2023, **14**, 84.

24 V. L. Deringer, M. A. Caro and G. Csányi, Machine learning interatomic potentials as emerging tools for materials science, *Adv. Mater.*, 2019, **31**, 1902765.

25 T. W. Ko and S. P. Ong, Recent advances and outstanding challenges for machine learning interatomic potentials, *Nat. Comput. Sci.*, 2023, **3**, 998.

26 S. Batzner, A. Musaelian, L. Sun, M. Geiger, J. P. Mailoa, M. Kornbluth, N. Molinari, T. E. Smidt and B. Kozinsky, E(3)-equivariant graph neural networks for data-efficient and accurate interatomic potentials, *Nat. Commun.*, 2022, **13**, 2453.

27 S. R. Xie, M. Rupp and R. G. Hennig, Ultra-fast interpretable machine-learning potentials, *npj Comput. Mater.*, 2023, **9**, 162.

28 A. P. Bartók, M. C. Payne, R. Kondor and G. Csányi, Gaussian approximation potentials: The accuracy of quantum mechanics, without the electrons, *Phys. Rev. Lett.*, 2010, **104**, 136403.

29 I. Batatia, D. P. Kovacs, G. Simm, C. Ortner and G. Csanyi, Mace: Higher order equivariant message passing neural networks for fast and accurate force fields, in *Advances in Neural Information Processing Systems*, ed. S. Koyejo, S. Mohamed, A. Agarwal, D. Belgrave, K. Cho, and A. Oh, Curran Associates, Inc., 2022, vol. 35, pp. 11423–11436.

30 G. Sivaraman, A. N. Krishnamoorthy, M. Baur, C. Holm, M. Stan, G. Csányi, C. Benmore and Á. Vázquez-Mayagoitia, Machine-learned interatomic potentials by active learning: amorphous and liquid hafnium dioxide, *npj Comput. Mater.*, 2020, **6**, 104.

31 C. G. Staacke, T. Huss, J. T. Margraf, K. Reuter and C. Scheurer, Tackling structural complexity in Li_2S-P_2S_5 solid-state electrolytes using machine learning potentials, *Nanomaterials*, 2022, **12**, 2950.

32 J. Zhao, J. Byggmästar, H. He, K. Nordlund, F. Djurabekova and M. Hua, Complex Ga_2O_3 polymorphs explored by accurate and general-purpose machine-learning interatomic potentials, *npj Comput. Mater.*, 2023, **9**, 159.

33 L. C. Erhard, J. Rohrer, K. Albe and V. L. Deringer, Modelling atomic and nanoscale structure in the silicon–oxygen system through active machine learning, *Nat. Commun.*, 2024, **15**, 1927.

34 H. Stöffler, T. Zinkevich, M. Yavuz, A. Senyshyn, J. Kulisch, P. Hartmann, T. Adermann, S. Randau, F. H. Richter, J. Janek, *et al.*, Li^{+}-ion dynamics in

β-Li_3PS_4 observed by NMR: local hopping and long-range transport, *J. Phys. Chem. C*, 2018, **122**, 15954.

35 H. Stöffler, T. Zinkevich, M. Yavuz, A.-L. Hansen, M. Knapp, J. Bednarcik, S. Randau, F. H. Richter, J. Janek, H. Ehrenberg, *et al.*, Amorphous versus crystalline Li_3PS_4: local structural changes during synthesis and Li ion mobility, *J. Phys. Chem. C*, 2019, **123**, 10280.

36 H. Tsukasaki, S. Mori, H. Morimoto, A. Hayashi and M. Tatsumisago, Direct observation of a non-crystalline state of Li_2S–P_2S_5 solid electrolytes, *Sci. Rep.*, 2017, **7**, 4142.

37 P. P. Man, Quadrupole couplings in nuclear magnetic resonance, general, *Encyclopedia of Analytical Chemistry*, 2000, vol. 10, DOI: **10.1002/9780470027318.a6111**.

38 J. Jeener and P. Broekaert, Nuclear magnetic resonance in solids: thermodynamic effects of a pair of rf pulses, *Phys. Rev.*, 1967, **157**, 232.

39 R. Böhmer, Multiple-time correlation functions in spin-3/2 solid-state NMR spectroscopy, *J. Magn. Reson.*, 2000, **147**, 78.

40 R. Böhmer, K. Jeffrey and M. Vogel, Solid-state Li NMR with applications to the translational dynamics in ion conductors, *Prog. Nucl. Magn. Reson. Spectrosc.*, 2007, **50**, 87.

41 G. Lipari and A. Szabo, Model-free approach to the interpretation of nuclear magnetic resonance relaxation in macromolecules. 1. theory and range of validity, *J. Am. Chem. Soc.*, 1982, **104**, 4546.

42 J. C. Mauro and Y. Z. Mauro, On the Prony series representation of stretched exponential relaxation, *Phys. A*, 2018, **506**, 75.

43 M. F. Graf, H. Tempel, S. S. Köcher, R. Schierholz, C. Scheurer, H. Kungl, R.-A. Eichel and J. Granwehr, Observing different modes of mobility in lithium titanate spinel by nuclear magnetic resonance, *RSC Adv.*, 2017, **7**, 25276.

44 A. P. Bartók, R. Kondor and G. Csányi, On representing chemical environments, *Phys. Rev. B: Condens. Matter Mater. Phys.*, 2013, **87**, 184115.

45 J. Behler and M. Parrinello, Generalized neural-network representation of high-dimensional potential-energy surfaces, *Phys. Rev. Lett.*, 2007, **98**, 146401.

46 A. Grisafi, D. M. Wilkins, G. Csányi and M. Ceriotti, Symmetry-adapted machine learning for tensorial properties of atomistic systems, *Phys. Rev. Lett.*, 2018, **120**, 036002.

47 A. F. Harper, S. Köcher, K. Reuter and C. Scheurer, Performance metrics for tensorial learning: prediction of $Li_4Ti_5O_{12}$ nuclear magnetic resonance observables at experimental accuracy, *ChemRxiv*, 2024, preprint, DOI: **10.26434/chemrxiv-2024-j0kp2**.

48 S. J. Clark, M. D. Segall, C. J. Pickard, P. J. Hasnip, M. I. Probert, K. Refson and M. C. Payne, First principles methods using CASTEP, *Z. Kristallogr. - Cryst. Mater.*, 2005, **220**, 567.

49 C. J. Pickard and F. Mauri, All-electron magnetic response with pseudopotentials: NMR chemical shifts, *Phys. Rev. B: Condens. Matter Mater. Phys.*, 2001, **63**, 245101.

50 S. W. Shepperd, Quaternion from rotation matrix, *J. Guid. Control Dyn.*, 1978, **1**, 223.

51 M. Sadowski and K. Albe, Computational study of crystalline and glassy lithium thiophosphates: Structure, thermodynamic stability and transport properties, *J. Power Sources*, 2020, **478**, 229041.

52 J. G. Smith and D. J. Siegel, Low-temperature paddlewheel effect in glassy solid electrolytes, *Nat. Commun.*, 2020, **11**, 1483, DOI: **10.1038/s41467-020-15245-5**.

53 M. A. Caro, Optimizing many-body atomic descriptors for enhanced computationalperformance of machine learning based interatomic potentials, *Phys. Rev. B*, 2019, **100**, 024112.

54 C. Dietrich, R. Koerver, M. W. Gaultois, G. Kieslich, G. Cibin, J. Janek and W. G. Zeier, Spectroscopic characterization of lithium thiophosphates by XPS and XAS – a model to help monitor interfacial reactions in all-solid-state batteries, *Phys. Chem. Chem. Phys.*, 2018, **20**, 20088.

55 M. Taches, J. Malugani, R. Mercier and G. Robert, Ionic conductivity of and phase transition in lithium thiophosphate Li_3PS_4, *Solid State Ionics*, 1984, **14**, 181.

56 K. Shimizu, P. Bahuguna, S. Mori, A. Hayashi and S. Watanabe, Enhanced ionic conductivity through crystallization of glass-Li3PS4 by machine learning molecular dynamics simulations, *J. Phys. Chem. C*, 2024, **128**(24), 10139–10145.

57 L. Gigli, D. Tisi, F. Grasselli and M. Ceriotti, Mechanism of charge transport in lithium thiophosphate, *Chem. Mater.*, 2024, **36**, 1482.

58 J.-S. Kim, W. D. Jung, J.-W. Son, J.-H. Lee, B.-K. Kim, K.-Y. Chung, H.-G. Jung and H. Kim, Atomistic assessments of lithium-ion conduction behavior in glass–ceramic lithium thiophosphates, *ACS Appl. Mater. Interfaces*, 2019, **11**, 13.

59 J. Granwehr and P. J. Roberts, Inverse Laplace Transform of Multidimensional Relaxation Data Without Non-Negativity Constraint, *J. Chem. Theory Comput.*, 2012, **8**, 3473.

60 B. Lee, K. Jun, B. Ouyang and G. Ceder, Weak correlation between the polyanion environment and ionic conductivity in amorphous Li–P–S superionic conductors, *Chem. Mater.*, 2023, **35**, 891.

61 M. Wilkening, A. Kuhn and P. Heitjans, Atomic-scale measurement of ultraslow Li motions in glassy $LiAlSi_2O_6$ by two-time ^6Li spin-alignment echo NMR correlation spectroscopy, *Phys. Rev. B: Condens. Matter Mater. Phys.*, 2008, **78**, 054303.

62 Y. Wang, W. D. Richards, S. P. Ong, L. J. Miara, J. C. Kim, Y. Mo and G. Ceder, Design principles for solid-state lithium superionic conductors, *Nat. Mater.*, 2015, **14**, 1026.

63 J. Granwehr, personal communication, 2024.